

# Target-free Stereo PIV: a novel technique with inherent error estimation and improved accuracy

Andreas Fouras · David Lo Jacono ·  
Kerry Hourigan

Received: 2 April 2007 / Revised: 19 September 2007 / Accepted: 25 September 2007 / Published online: 19 October 2007  
© Springer-Verlag 2007

**Abstract** A novel, accurate and simple stereo particle image velocimetry (SPIV) technique utilising three cameras is presented. The key feature of the new technique is that there is no need of a separate calibration phase. The calibration data are measured concurrently with the PIV data by a third paraxial camera. This has the benefit of improving ease of use and reducing the time taken to obtain data. This third camera also provides useful velocity information, considerably improving the accuracy of the resolved 3D vectors. The additional redundancy provided by this third perspective in the stereo reconstruction equations suggests a least-squares approach to their solution. The least-squares process further improves the utility of the technique by means of the reconstruction residual. Detailed error analysis shows that this residual is an accurate predictor of resolved vector errors. The new technique is rigorously validated using both pure translation and rotation test cases. However, while this kind of validation is standard, it is shown that such validation is substantially flawed. The case of the well-known confined vortex breakdown flow is offered as an alternative validation. This flow is readily evaluated using CFD methods, allowing a detailed comparison of the data and evaluation of PIV errors in their entirety for this technique.

## 1 Introduction

Stereo particle image velocimetry (SPIV) is now a well-established extension of traditional PIV (Arroyo and Greated 1991; Willert 1997; Prasad 2000). SPIV offers several advantages over standard (or planar) PIV in addition to the resolution of the out-of-plane components. These advantages include the improved accuracy of in-plane components of the velocity field due to removal of perspective error. Recent extensions of SPIV include three-dimensional (3D) high-speed scanning (Hori and Sakakibara 2004), multi-plane SPIV (Schroder and Kompenhans 2004), dual-time SPIV for acceleration measurement (Perret et al. 2006), and stereoscopic micro-PIV (Lindken 2006).

The three-component velocity field is reconstructed based on two velocity fields derived from PIV. This reconstruction process relies on both geometrical equations based on the camera setup, and a calibration step linking the acquired image plane to the object plane.

Following the terminology of Prasad (2000), several techniques exist in order to reconstruct the 3D velocity field from distorted 2D fields, namely geometric reconstruction (Prasad and Adrian 1993), 2D calibration-based reconstruction and 3D calibration-based reconstruction (Soloff et al. 1997).

The calibration based methods correct the unavoidable distortion from the image plane. The difference between two- and 3D techniques is that the latter also involves calibration from the object plane to a number of parallel planes near the imaging plane. These additional calibrations indirectly provide the information relating to the imaging geometry (Prasad 2000; Prasad and Adrian 1993; Raffel et al. 1998; Soloff et al. 1997). These calibration based methods are sensitive to alignment errors in the

---

A. Fouras (✉) · D. Lo Jacono · K. Hourigan  
Fluids Laboratory for Aeronautical and Industrial Research  
(FLAIR), Division of Biological Engineering,  
Monash University, PO Box 31,  
Clayton, VIC 3800, Australia  
e-mail: fouras@eng.monash.edu.au

positioning of the calibration plate relative to the measurement plane. However, as described by Willert (1997) and furthered by Wieneke (2005) and Fouras et al. (2007), cross-correlation between cameras (of particle images taken at the same instant) can also provide calibration information. For example, Wieneke (2005) provides a system to use this information to provide correction for misalignment of the calibration plate.

Almost all calibrations utilise a target, which consists of a discrete number of markers placed on a regular Cartesian grid (Lawson and Wu 1997). Typically, these targets contain in the order of 100 such markers, i.e.,  $10 \times 10$  grid. The exact method of undertaking this calibration varies depending on the Stereo PIV software being utilised. However, it is largely based on the PIV algorithms themselves and may even require the practitioner to manually identify markers in an image and link them to a corresponding marker on the target. The uncertainty in identifying the position of these markers by use of PIV software is proportional to the size of these markers. The calibration data are then fitted to a polynomial function by least-square means (both linear and non-linear are used).

A technique that offers the advantages of the above techniques, with even greater improvements in reconstruction accuracy and without the requirement of the practitioner to conduct a distinct calibration phase, has been developed based on the work by Fouras et al. (2007). This calibration target free technique utilises a third camera placed in the paraxial (normal to the light sheet) position. This technique is of greatest utility when the paraxial view has minimal distortion or when it is not convenient to place a calibration target in the measurement region. The paper will be divided as follows: a description of the three camera technique; followed by an experimental validation and an extensive error analysis will be presented. The paper concludes with a comparison of Stereo PIV measurements using the novel technique and CFD of a confined vortex breakdown.

## 2 Description of novel technique

Before PIV interrogation of the image pairs begins, PIV interrogation of the images captured at the same instant is undertaken to determine the distortion or calibration map. The calibration map can be acquired with an accuracy far outstripping that of any discrete system of large markers. This is for two reasons. First, the ability to accurately determine the position of any object is proportional to the size of that object and PIV particles are smaller than the markers on calibration targets. Second, the calibration data can be averaged over the entire series of data acquired under the same stereo imaging parameters. This means that

as the number of PIV measurements increases, the RMS error of the calibration maps approaches zero. Faster convergence to this zero error state can be achieved by the use of correlation averaging (Meinhart et al. 2000). Rather than averaging instantaneous vector fields, this technique involves averaging the cross-correlation function before the peak is determined.

In addition, further improvement is made by making use of the information provided by the third paraxial camera. During the reconstruction phase, there is now considerably more information available than for typical two camera SPIV. A definition of the key spatial variables can be found in Fig. 1. Standard reconstruction solves four equations ( $\delta x$  and  $\delta z$  component of the displacement vector from two cameras) with three unknown terms ( $\delta x$ ,  $\delta y$  and  $\delta z$  components of the reconstructed vector). In reality, however, the solution of the  $\delta x$  and  $\delta z$  components of the reconstructed vector are almost completely de-coupled from the solution of the  $\delta y$  component. (Here, as shown in Fig. 1, the plane in which the cameras lie is the  $xz$  plane.) This means that the solution of the  $\delta y$  component is, to a large extent, simply the average of the  $\delta y$  component from each camera and that the solution of the  $\delta x$  and  $\delta z$  components of the reconstructed vector is fully constrained problem with two equations and two unknowns. With data available from the third camera, there are now six equations. This allows not only further averaging for the  $\delta y$  component, (reducing errors to  $\sqrt{2/3}$  of the level with two cameras), but also now allows for a least-square solution of the  $\delta x$

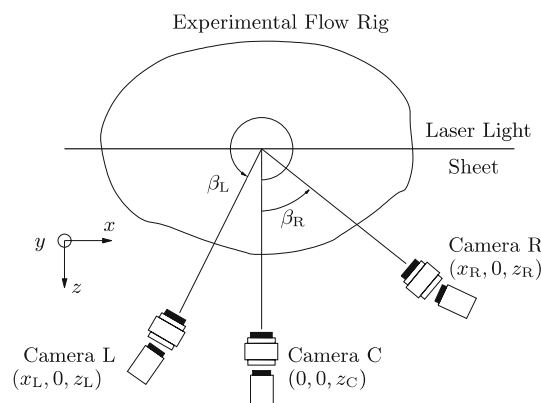


**Fig. 1** Schematic diagram of generic Stereo PIV (SPIV) configuration including the co-ordinate systems used in this paper. Shown on the figure are the  $x$ ,  $y$  and  $z$  axes. The origin of the coordinate system is the point on the laser sheet plane in the center of the imaged region of interest, from the central camera denoted camera C. Also, two additional cameras, denoted left (L) and right (R) for simplicity are shown. Also shown is the Scheimpflug configuration and the definition of the camera angles  $\beta_L$  and  $\beta_R$ , as well as their positions  $(x_L, 0, z_L)$  and  $(x_R, 0, z_R)$ . The paraxial camera (camera C) is held at the angle ( $\beta_C = 0$ ) and at a fixed position  $(0, 0, z_C)$  throughout the paper

and  $\delta z$  components with three equations and two unknowns, once again improving accuracy.

The additional information also increases the redundancy contained within the system. In other SPIV systems, if the data from one image are unavailable for some reason during the reconstruction process, such as data rejection during PIV interrogation, a hole appears in those data, as two geometric equations will not suffice to solve for all three unknowns. In the three camera case, if data are unavailable from one camera, then a solution from the remaining two cameras is still viable. The effects of this redundancy grow dramatically with increasing vector failure rates. For the case of 5% vector failure rates, a standard two camera stereo will suffer a failure rate of 9.75%, whereas a three camera technique will only suffer a 0.75% failure rate.

Along with a definition of the key spatial variables, a typical camera configuration for the three camera stereo technique can be found in Fig. 1. The origin of the angles is defined by the paraxial or central camera (here defined as camera C). The practitioner is free to move the cameras to any configuration they choose. This includes the popular arrangement where cameras are symmetrically placed about the laser sheet as opposed to being symmetrically placed about the paraxial position as shown in the schematic.

The entire Stereo PIV technique is described schematically in Fig. 2. All PIV interrogation is performed in real world co-ordinates as measured by the paraxial camera C. This means that measured data are directly utilised in the reconstruction process without the need for any interpolation. To achieve this, mapping functions (MF) for the co-ordinate systems as measured by the stereographic cameras, relative to the paraxial camera, are required. These MFs are directly measured by cross-correlating the images from the paraxial camera with matching images (taken at the same instant in time) from each stereographic camera in turn. These MFs are simply the displacement vector fields of apparent motion of particles as a result of differences of perspective between cameras. It should be noted that, unlike other target based systems where the number of points in the system is limited (i.e., generally in the order of 100), here the number of points is equal to the number of vectors to be sought (typically in the order of  $64 \times 64 = 4,096$ ). These MFs are now used as inputs into the window shifting function (WS) of the PIV software developed by the authors (see CC loop in Fig. 2, right). The displacement vector fields caused by the fluid motion as measured from each of the three perspectives are now measured. Almost all modern PIV software performs WS to improve accuracy and dynamic range. The accuracy can be still further improved by symmetrically shifting both

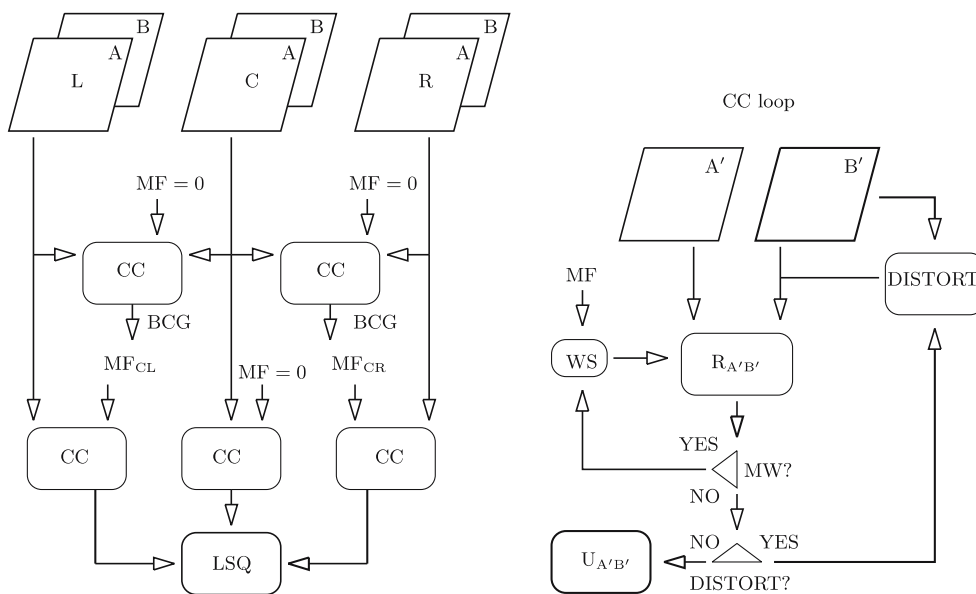


**Fig. 2** Schematic diagram showing (left) the proposed target-free, three camera Stereo PIV process. Inputs are the image pair sets (denoted A and B) from the three cameras (here denoted L, C and R). Each set is cross-correlated with the paraxial set (here C) in the CC loop in order to generate the corresponding mapping functions (MF). These MFs will in turn be used as inputs for the window shifting (WS) for the cross-correlation of each set. Finally, the

displacement fields of each set are used in a least-square geometric reconstruction method (LSQ) to generate the three component vector field. Also shown (right) is the cross-correlation process (CC loop) including WS based on the MF and multi-window iteration (MW). To reduce peak-locking in the sub-pixel component, an additional distortion loop is included

windows to achieve the same relative displacement (Meunier and Leweke 2003). The only special feature of the PIV software required to perform this calibration is to accept as an input to the displacement vector field of the MF and to displace both windows in the cross-correlation analysis by this amount.

By including the MF into the technique in this way, the requirement to interpolate the data (either the image before the PIV interrogation or the vectors after) is avoided provided the MF data are calculated on the same grid as that on which the flow is to be measured. This grid is defined from the perspective of the paraxial camera.

It can be seen in Fig. 2 that particle image distortion (PID) is employed to reduce peak locking. This PID is used globally (i.e., on the entire image) and not locally (i.e., PIV interrogation window). The interpolation scheme chosen is a bi-cubic interpolation as used by Chen and Katz (2005). The effects of the first pass of PID are shown in Fig. 3.

Specifically in the case of the MFs, peak locking errors may be completely eradicated by replacing the measured data with an analytical representation. This not only removes peak locking but any remaining random errors. The authors wish to stress that PIV random errors will be small because of the averaging process described earlier and that analytical representation is not necessarily required. In this case a cubic representation was chosen. The choice of a cubic dependence in  $x$  and  $y$  is arbitrary and chosen for its simplicity and high performance (Soloff et al. 1997).

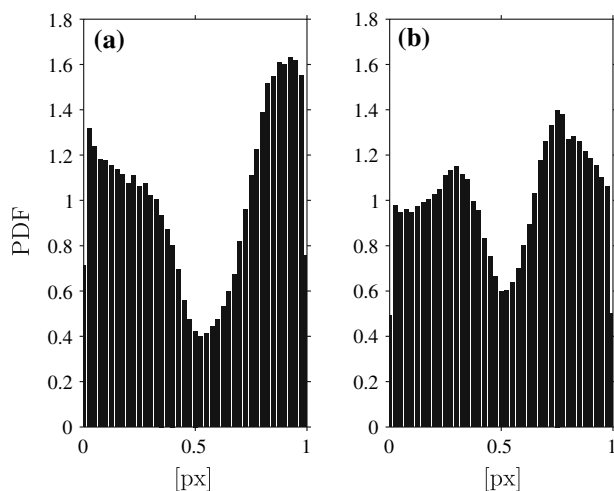


**Fig. 3** **a** Probability density function (*PDF*) of typical sub-pixel component of cross-correlation process. **b** *PDF* after second image pair is globally distorted by resultant displacement field using bi-cubic interpolation scheme. The figure shows the extent of the peak locking and reduction caused by distortion process

$$\text{MF}(x, y) = a_0 + a_1x + a_2x^2 + a_3x^3 + a_4xy + a_5x^2y + a_6xy^2 + a_7y + a_8y^2 + a_9y^3, \quad (1)$$

where  $\mathbf{a}_i$  are vector valued coefficients to be determined. Because of the large number of points, a least-squares solution by means of a bi-conjugate gradients method (BCG) has been used to determined the coefficients (Press et al. 1992).

Finally, each of the three displacement fields is used in a least-squares geometric reconstruction method (LSQ) to generate the three component vector field on a point by point basis. This is achieved by using the standard pinhole model at each location on the element grid, since each displacement vector field is calculated in the same coordinates as the paraxial or center camera. The least-square solver is implemented with singular value decomposition as described in Press et al. 1992). More precisely, the above formulation can be expressed as follows:

$$\begin{bmatrix} 1 & 0 & (\Delta x_1 - x_1)/z_1 \\ 0 & 1 & (\Delta y_1 - y_1)/z_1 \\ \vdots & \vdots & \vdots \\ 1 & 0 & (\Delta x_N - x_N)/z_N \\ 0 & 1 & (\Delta y_N - y_N)/z_N \end{bmatrix} \begin{bmatrix} \delta_x \\ \delta_y \\ \delta_z \end{bmatrix} = \begin{bmatrix} \Delta x_1 \\ \Delta y_1 \\ \vdots \\ \Delta x_N \\ \Delta y_N \end{bmatrix} \quad (2)$$

where  $(x_i, y_i, z_i)$  and  $(\Delta x_i, \Delta y_i) = (gx_c + \delta_{x_i}, gy_c + \delta_{y_i})$  are the position and the measured projection of the  $i$ th camera (measured  $\delta_{x_i}$  displacement added with the grid position  $(gx_c, gy_c)$  from the center of the center camera for varying viewing angle across the image), respectively; and  $N$  is the total number of cameras used.

Alternatively, instead of a pinhole model and a single plane calibration technique, a practitioner employing a more widely used technique such as that proposed in Soloff et al. (1997) could utilise many of the advantages described in this paper by making only minor changes to their practice. These changes would include calibrating by traversing the light sheet through their measurement volume and solving the reconstruction equations with a least-squares method.

### 3 Validation

The performance of the three camera technique was investigated initially with two separate experiments undertaken to test the ability of the new system to measure the classical test cases of pure translation and pure, solid-body rotation. Only a brief overview is given here, since a detailed description of these experiments can be found in Fouras et al. (2007), with the primary difference that three cameras were used in this case as opposed to the standard configuration of two cameras in that work.

The translation experiments were carried out using two different symmetric camera angles, as SPIV system performance often varies with the camera positions (Lawson and Wu 1997). Camera angles of  $\beta_R = -\beta_L = 30^\circ$ , and  $\beta_R = -\beta_L = 45^\circ$  were chosen, as these represent typical offsets that produce significant image distortion. The flow field was simulated by a sheet of paper printed with a pseudo-random pattern. This paper was fixed between glass plates and attached to a linear traverse driven by a precision ground lead screw driven by a geared stepper motor. The object was positioned for each image using a micro-stepping, stepper motor controller. Images were recorded at 101 positions with a small known displacement between each image. This allowed a flexible system of analysis; by interrogating against different pairs, different length vectors were achieved. Different vector lengths ( $k\delta x$ :  $k = 1, 16$ ) were obtained by analysing  $CC(i, i + k)$ , where  $i$  is the frame number,  $k$  is the number of skipped frames, and  $CC$  is the cross-correlation process (see Fig. 2). In this manner, 16 reliable data sets of increasing magnitude were obtained. Since image quality and other PIV acquisition and processing parameters were held constant, PIV errors were also held constant in absolute terms. By normalising each data set by the known displacement, 16 data sets with varying levels of PIV accuracy were achieved.

The rotational test cases were performed by rotating a fluid body within a cylindrical vessel. The vessel was first accelerated to a constant rotational rate of  $\omega_1 = \pi/4$  rad/s, and the relative fluid motion allowed to decay resulting in solid-body rotation. The rate of decay and the continued damping of any relative fluid motion were enhanced by the use of a glycerine/water mixture as the working fluid. In a manner similar to the translation case, this whole data set was analysed twice to produce data with apparent rotation rates of  $\omega_1 = \pi/4$  rad/s and  $\omega_2 = \pi/2$  rad/s.

As the theoretical displacements of the translation and rotation test cases are known, statistics can be compiled regarding errors relative to these theoretical values. The theoretical values for the rotation case are based on the known rotation rate, with the center of rotation determined by least-squares fit. The global values for bias ( $\mu$ ) and standard deviation ( $\sigma$ ), associated with the  $45^\circ$  translation case (with  $k = 16$  corresponding to  $\delta x = 33.95$  px) and the  $\omega_1$  rotation case are outlined in Table 1. The values are expressed in pixels and represent a combination of the accuracy of the PIV as well as the stereo reconstruction process. The values demonstrate that all three displacement vector components were evaluated with a high degree of precision.

Detailed results from the rotational test cases are displayed in Fig. 4. The figure shows the out of plane displacements  $\delta z_1$ ,  $\delta z_2$  plotted as a function of  $r^*$ , the normalised radial position for  $\omega_1 = \pi/4$  and  $\omega_2 = \pi/2$  rad/s.

**Table 1** Table of numerical values of bias ( $\mu$ ) and standard deviation ( $\sigma$ ) associated with the  $\omega_1$  case shown in Fig. 4

	$\mu$	$\sigma$
Translation case (%)		
$\delta x$	2.12	1.15
$\delta y$	-1.21	0.71
$\delta z$	0.61	1.88
Rotation case ( $10^{-2}$ px)		
$\delta x$	1.01	5.41
$\delta y$	0.96	6.35
$\delta z$	NA	7.01

As the center of rotation was fitted, the bias value for  $\delta z$  is necessarily zero and hence is not included

Solid lines indicate the theoretical  $\delta z_{(1,2)}$  values. Error bars show the localised (for each  $r^*$ ) standard deviation of the measured values when compared to the theoretical ones. The error bars clearly show that the relative errors are small and do not vary significantly over the radius.

Figure 5 shows the probability density function (PDF) of errors associated with  $\delta z_1$  case shown in Fig. 4. The error is simply the difference between the measured and the theoretical value. The theoretical values of  $\delta x$  and  $\delta y$  are assumed to be zero. The solid lines shown in Fig. 5 indicate Gaussian curves with standard deviations and means taken from Table 1. The PDF envelopes closely match Gaussian profiles indicating the Gaussian nature of the errors. This information is of importance and will be utilised in the error analysis of Sect. 4.

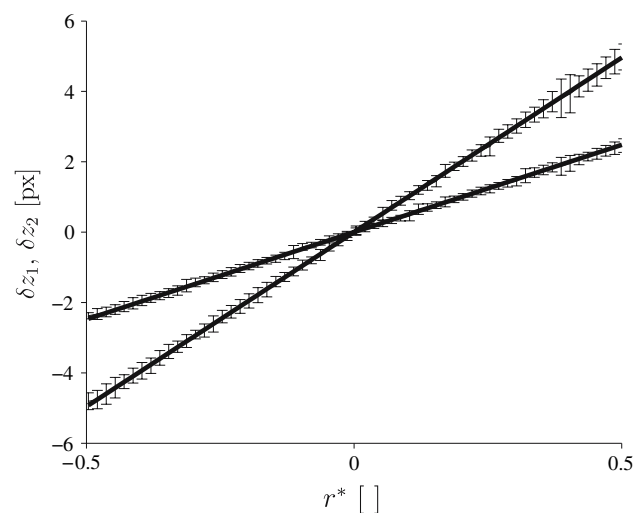


**Fig. 4** Out of plane displacement components  $\delta z_1$  and  $\delta z_2$  plotted as a function of  $r^*$ , the normalised radial position, for the rotational cases of  $\omega_1 = \pi/4$  rad/s and  $\omega_2 = \pi/2$  rad/s, respectively. Solid lines indicate theoretical  $\delta z_{(1,2)}$  values based on these rotation rates, with the center of rotation determined by least-squares fit. Error bars show the standard deviation of the measured values when compared to the theoretical ones

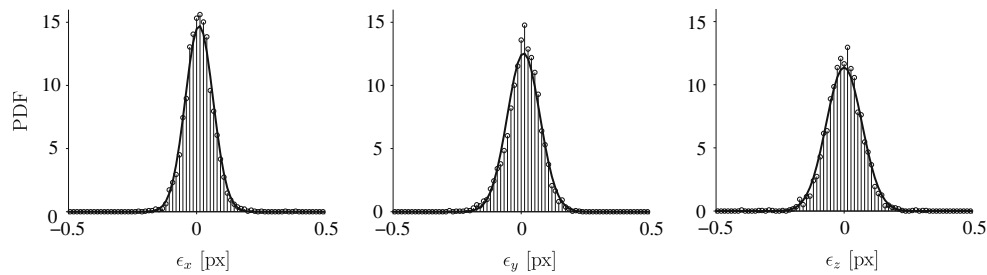


**Fig. 5** Probability density function of errors (denoted  $\epsilon = (\epsilon_x, \epsilon_y, \epsilon_z)$ ) for each of three components associated with  $\omega_1$  case shown in Fig. 4. Theoretical values of  $\delta x$  and  $\delta y$  are assumed to be zero. *Solid lines*

Table 2 shows the changes in the statistics shown in Table 1 with one of the MFs set to null. The changes are typically less than 2%. The results clearly show the insensitivity to changes in the MF and hence the calibration technique. The insensitivity of these results to very large errors in the MF calls into question the very practice of using these classical test cases to validate SPIV techniques. The authors believe that other more complex test cases are required to properly validate SPIV techniques. This is supported by the findings of Scarano et al. (2005) that a truly 3D flow configuration is required to fully test their stereo configurations. One alternative validation case is discussed in Sect. 5.

#### 4 Error analysis

Several authors have derived error analysis from the equations of the reconstruction process. The current technique differs from those techniques in that the reconstruction process is a least-squares process and while analytical error analysis of a least-squares process is possible (Fouras and Soria 1998), it is limited and not straightforward. In this case, it is more appropriate to perform a Monte Carlo simulation to assess the sensitivity

**Table 2** Table of numerical values of relative changes to bias ( $\Delta\mu$ ) and standard deviation ( $\Delta\sigma$ ) associated with the translation and rotation case when one of the MFs are set to null

	$\Delta\mu$ (%)	$\Delta\sigma$ (%)
Translation case		
$\delta x$	1.90	0.03
$\delta y$	0.20	<0.01
$\delta z$	4.90	0.02
Rotation case		
$\delta x$	0.98	1.13
$\delta y$	0.32	1.97
$\delta z$	0.07	0.17

indicate Gaussian curves with matching values for the standard deviation and mean. Error data closely match Gaussian profiles indicating the Gaussian nature of the errors

of the reconstructed 3D vector errors to the multiple input 2D vector errors.

The input errors will be denoted as  $\epsilon_{in}$ , which are the two component random displacement errors as viewed from each camera. The standard deviation of  $\epsilon_{in}$  is defined as  $\sigma_{in} = (\sigma_{in}^x, \sigma_{in}^y) = \sigma(\epsilon_{in})$ . A variable  $\sigma_{piv}$  which represents the PIV measurement error of a single component as measured by the paraxial camera is used here. Because vector errors are proportional to particle image size, component stereographic displacement vectors have the following errors relative to  $\sigma_{piv}$ :

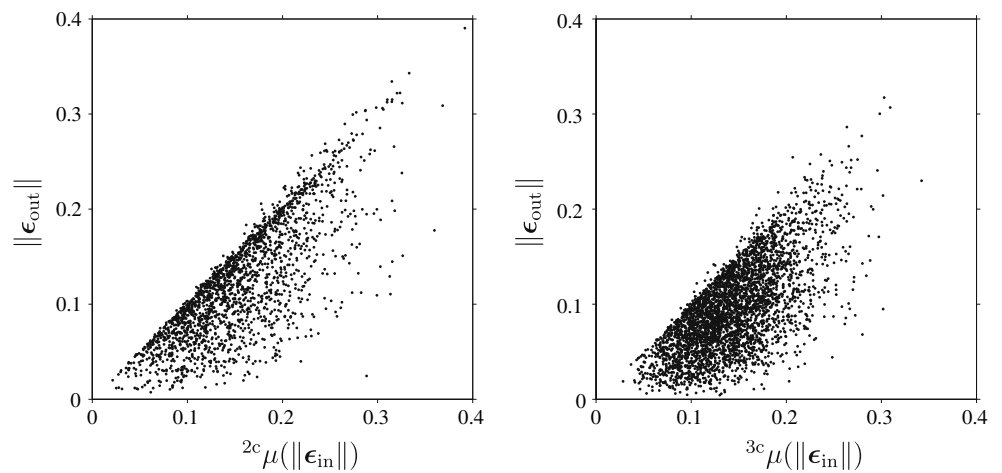
$$\begin{aligned}\sigma_{in}^x &= \sigma_{piv} / \cos(\beta), \\ \sigma_{in}^y &= \sigma_{piv}.\end{aligned}\quad (3)$$

The output errors will be denoted as  $\epsilon_{out}$ , which is the three component reconstructed displacement error. The standard deviation of  $\epsilon_{out}$  is defined as  $\sigma_{out} = (\sigma_{in}^x, \sigma_{in}^y, \sigma_{in}^z) = \sigma(\epsilon_{out})$ .

Monte Carlo simulations were performed by creating displacement vector fields with pseudo-random Gaussian distributions. It was then confirmed that similar to the errors shown in Fig. 5, the output errors were Gaussian and proportional to the input errors. As a result, we are freed to investigate the sensitivity or the ratio of the output error to the input error at any arbitrary input error level. All further simulations were conducted with the arbitrary input error of  $\sigma_{piv} = 0.1$  px with  $\delta x$  and  $\delta y$  component errors dictated by equations (Eq. 3). The left and right displacement fields were used with and without the center camera displacement field, to simulate both two and three camera technique sensitivities, respectively.

The base case for these Monte Carlo simulations was the symmetric 45° camera configuration. Figure 6 shows the result of 3,600 samples (4% of total data volume used for statistics) of the Monte Carlo simulation for the base case. Shown in the figure is the mean (averaged across two or three cameras as appropriate) of the norm of the input errors,  $\mu(\|\epsilon_{in}\|)$ , versus the norm of the reconstructed errors,  $\|\epsilon_{out}\|$ , for both two and three cameras, denoted with the superscript 2c and 3c, respectively. In both cases, an

**Fig. 6** Scatter plot of the norm of the mean of the norm of the input errors,  $\mu(\|\epsilon_{in}\|)$ , versus the norm of the reconstructed errors,  $\|\epsilon_{out}\|$ , for two and three cameras (denoted with the superscript 2c and 3c, respectively) on the left and right, respectively



upper bound on the  $\|\epsilon_{out}\|$  data is apparent. This indicates that all cases of a high output error are the result of a high input error. A linear fit to each scatter plot yields values for the residual of 0.625 and 0.467 for two and three cameras, respectively. This signifies that high values of input errors are less likely to result in high values of output errors in the three camera case than for the two camera case. This is further evidenced by the fact that, overall, the  $\|\epsilon_{out}\|$  data are lower for the three camera case than the two camera case.

Wieneke (2005) utilised the residual of the reconstruction process to identify errors in the input displacement vectors; these data are then rejected from the process. This is an interesting idea worth investigating. Figure 7 shows the results from the same Monte Carlo simulation, as discussed above, as a scatter plot of the square-root of the residual of reconstruction,  $\chi = \sqrt{\chi^2}$ , versus the mean of the norm of the input errors ( $\mu(\|\epsilon_{in}\|)$ ) for two and three cameras on the left and right, respectively. For the two camera data (on the left), the solid line follows  $\mu(\|\epsilon_{in}\|) = \sqrt{2}\chi$ . In this figure, we can see that for the case of two cameras the data are upper bound by the line

$\mu(\|\epsilon_{in}\|) = \sqrt{2}\chi$  but only weakly correlated. This indicates that using the residual as an indicator of input errors would be inaccurate and unreliable. For example, a low value of  $\chi$  does necessarily correspond to a low value of  ${}^{2c}\mu(\|\epsilon_{in}\|)$ . However, a high value of  $\chi$  does not at all necessarily correspond to a high value of  ${}^{2c}\mu(\|\epsilon_{in}\|)$ . While this indicator is not reliable for the two camera case, for three cameras the data were more strongly correlated (the line of best fit indicated by the solid line). This means that the indicator is in general more accurate. This is manifested in the fact that a high value of  $\chi$  corresponds to an increased probability of a high value of  ${}^{3c}\mu(\|\epsilon_{in}\|)$ . However, it must be noted that even in the three camera case, the reconstruction residual is not reliable on an individual, point-by-point, basis.

It is also interesting to investigate the possible correlation between the residual of the reconstruction process with errors in the reconstructed vector. Figure 8 shows the results from the same Monte Carlo simulation, discussed above, as a scatter plot of the residual of reconstruction,  $\chi$ , versus the norm of the output errors ( $\|\epsilon_{out}\|$ ) for two and three cameras on the left and right, respectively. Note that

**Fig. 7** Scatter plot of the residual of reconstruction,  $\chi$ , versus the norm of the input errors,  $\|\epsilon_{in}\|$ , for two and three cameras (denoted with the superscript 2c and 3c, respectively) on the left and right, respectively. The solid lines on the graphs follow  $\|\epsilon_{in}\| = \sqrt{2}\chi$  and the line of best fit for the left and right, respectively

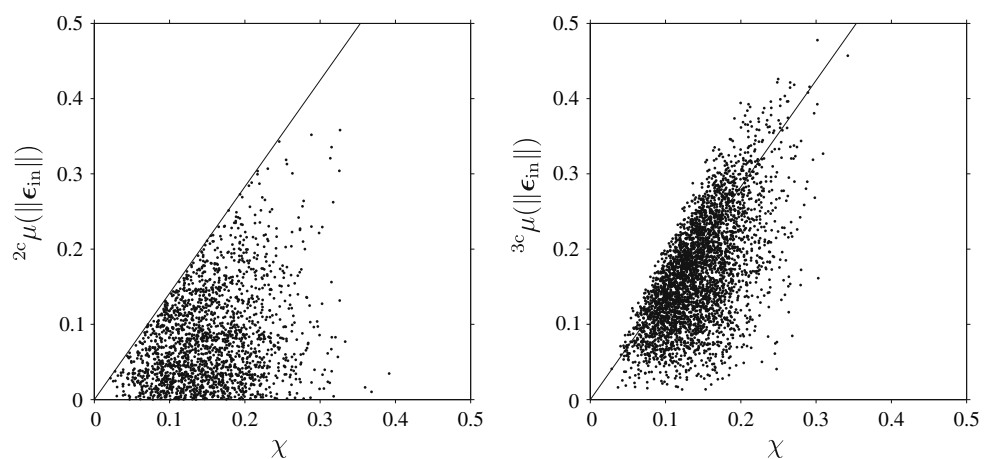
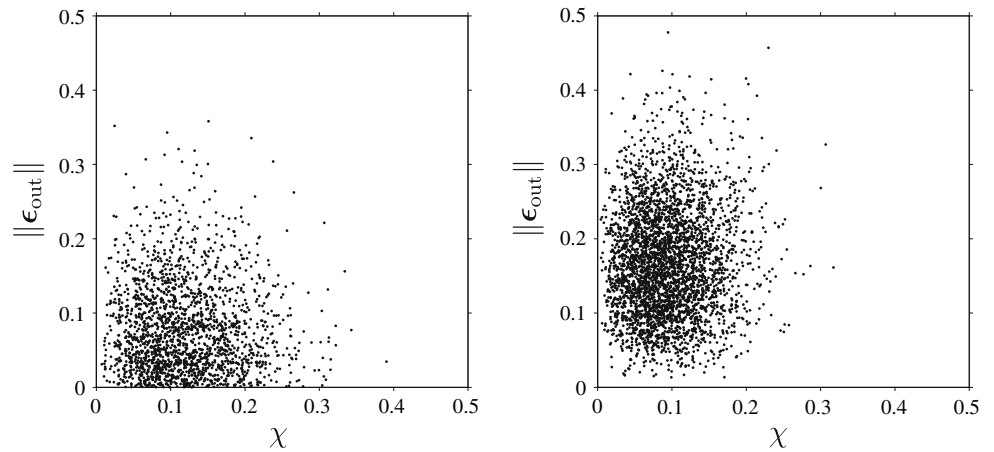


**Fig. 8** Scatter plot of the residual of reconstruction,  $\chi$ , versus the norm of the reconstruction errors,  $\|\epsilon_{out}\|$ , for two and three cameras on the left and right, respectively. Note that in the case of two cameras, the data are completely uncorrelated, while for the case of three cameras the scatter plot shows only very weak correlation which indicates that there is little value in using  $\chi$  as a metric of the output error on a point-by-point basis



in the case of two cameras, the data are completely uncorrelated, and that for the three camera configuration the scatter plot shows only very weak correlation. This signifies that there is little value in using  $\chi$  as a metric of the output error on a point-by-point basis.

What is significant, however, is that while these values are not very well correlated to each other on a point-by-point basis, on an ensemble or global basis the correlation is perfect. Figure 9 illustrates the perfect correlation between  $\chi$  and both the input errors  $\sigma_{piv}$  and output errors  $\|\sigma_{out}\|$  for a 45° camera setup. This suggests that when the pinhole model reconstruction equations are solved using a least-squares method, the global mean of the residual,  $\chi$ , may be used as an indicator of not only the input errors, but more usefully, the errors in the reconstructed vectors.

Several further points can be made about the data in Fig. 9. The unity slope in the log–log plot indicates that the relationship between  $\mu(\chi)$  and the input and output errors is linear. Furthermore, the slightly greater difference between  $\sigma_{piv}$  and  $\|\sigma_{out}\|$ , on the left figure compared to the right shows that the three camera technique is less sensitive to input errors.

The data from the Monte Carlo simulation can now be analysed to calculate the sensitivity of the least-squares reconstruction process, by comparing the global standard deviation of the outputs errors and the reconstruction residual to the global standard deviation of the input errors  $\sigma_{piv}$ . This analysis can be repeated for all values of  $\beta_L$  and  $\beta_R$ . The results of these simulations can be seen in Fig. 10.

For the  $\delta x$  projection, Fig. 10a, the sensitivity to input errors is lowest when the cameras are placed close to the paraxial position and symmetrically opposed to each other (or the opposite paraxial position). However, in this case, there appears a second area of low sensitivity along the line of  $\beta_L = \beta_R$ . This counter-intuitive result can be explained by the presence of the paraxial camera and the fact that along this line, the errors on stereographic cameras will cancel. This analysis assumes that errors are independent variables and ignores the impracticality of conducting experiments with  $\beta_L \approx \beta_R$ . One final point to note is that the sensitivity results shown are significantly less than those for two cameras reported in Fouras et al. (2007) and Lawson and Wu (1997).

**Fig. 9** For a 45° camera setup, several magnitudes of random error,  $\sigma_{piv}$ , were introduced. Plotted against the global mean of the square-root of  $\chi^2$  ( $\mu(\chi)$ ) are  $\sigma_{piv}$  (square) and  $\|\sigma_{out}\|$  (circle) showing a perfect dependency for both two camera (left) and three camera (right) configurations. The solid line follows a linear best fit

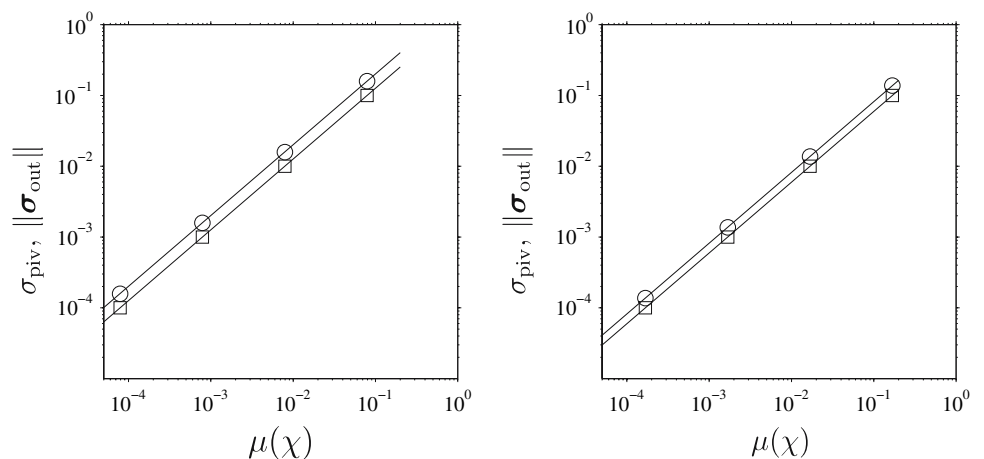
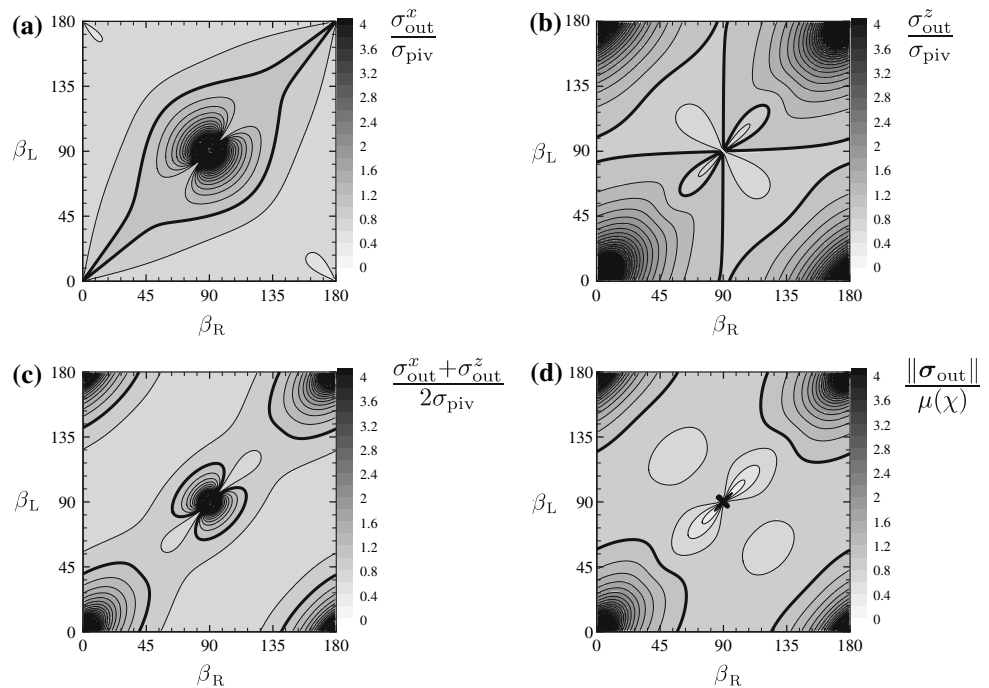




**Fig. 10** Sensitivity of the three camera technique calculated by numerical Monte Carlo analysis as a function of camera angles with one camera fixed at the paraxial position (camera C). **a, b** Show the sensitivity of the  $x$  and  $z$  components. **c** is the average of **a** and **b**. **d** Shows the global mean of the residuals from the least-square solution ( $\mu(\chi)$ ) of the 3D vector reconstruction. The **bold line** indicates the boundary of the iso value equal to 1.0, and the iso-values vary in steps of 0.2



Logically the next quantity to examine for sensitivity is  $\delta y$ . This is not shown in the figure, since the result is trivial. The reconstructed  $\delta y$  component is effectively always equal to the average of the  $\delta y$  measurements from each of the stereographic cameras. This results in the values for the sensitivity of  $1/\sqrt{2}$  for two cameras and  $1/\sqrt{3}$  for three cameras.

Along the  $\delta z$  projection, Fig. 10b, the sensitivity to input errors is the lowest when the cameras are placed far from the paraxial position (i.e., close to the laser position) and symmetrically opposed to each other (or the opposite paraxial position). Again in this case appears a second area of low sensitivity along the line of  $\beta_L = \beta_R$ , for which an explanation similar to that for the  $\delta x$  projection is viable.

The form of Fig. 10c, showing the measure of the average of  $\sigma_{out}^x$  and  $\sigma_{out}^z$ , is readily explained via the results of the components. Of interest is that, while similar to the two camera case (Fouras et al. 2007) with a minimum along the line of  $\beta_L - \beta_R = 90^\circ$  (which includes the symmetric case of  $\beta = \pm 45^\circ$ ), there is a very broad minimum along a curved line near to  $\beta_L - \beta_R = 90^\circ$ . In this case the minimum lies at  $\beta = \pm 50^\circ$ . This broader stereo angle is explained by the reduction in the  $\delta x$  error, affording more significance to the  $\delta z$  component, which is reduced by broader stereo angles.

Finally, in Fig. 10d, we can see a plot of  $\|\sigma_{out}\|/\mu(\chi)$  as a function of  $\beta_L$  and  $\beta_R$ . The authors wish to stress that by calculating this value for their experimental configuration, a practitioner has direct access to an effective estimate of both their input and output errors. The practitioner simply has to calculate the ensemble average of the residual  $\chi$  of

the least-squares reconstruction process, multiply this value by the gradient value and they have this accurate indication of the errors of a particular set of stereo measurements. This is without any theoretical or computational estimate of the displacement or velocity field. An example application of this predictor will be presented in Sect. 5.

As described in Sect. 3, the methodology undertaken to test the SPIV technique for translation cases allowed the level of PIV accuracy to be controlled. By varying the displacement of the target between images, 16 different values of  $\sigma_{in}^x$ , the standard deviation of the PIV processing error,  $\sigma_{piv}$ , were achievable. This facilitated a comparison between the standard deviation of the reconstructed stereo error,  $\|\sigma_{out}\|$ , and  $\sigma_{piv}$ . The solid lines follow the theoretical prediction taken from the error analysis shown in Fig. 10. This further verifies this analysis as the agreement between experimental values and Monte Carlo simulation are excellent.

These results are significant not only for their validation of the Monte Carlo simulation but also when compared to the results of other papers that describe this sensitivity for standard two camera stereo techniques. A complete error analysis for the standard two camera stereo system is performed in Fouras et al. (2007). For the symmetric case (as is displayed in Fig. 11), the same results have also been reported by Lawson and Wu (1997). In Table 3 the results for the cases of  $\beta_L = -\beta_R = 30^\circ$  and  $\beta_L = -\beta_R = 45^\circ$  are compared with the results calculated in Figs. 10 and 11. The results for the two cameras show perfect agreement with the published values in Fouras et al. (2007) and Lawson and Wu (1997) which both utilise different techniques. Significant

**Fig. 11** Sensitivity of the three camera technique measured with  $\beta_L = -\beta_R = 30^\circ$  (left) and  $\beta_L = -\beta_R = 45^\circ$  (right). Measurements taken on the translation experiment with 16 different displacements. Diamond and square symbols represent  $\sigma_{out}^x$  and  $\sigma_{out}^z$ , respectively. Associated solid lines follow the theoretical prediction taken from the error analysis shown in Fig. 10

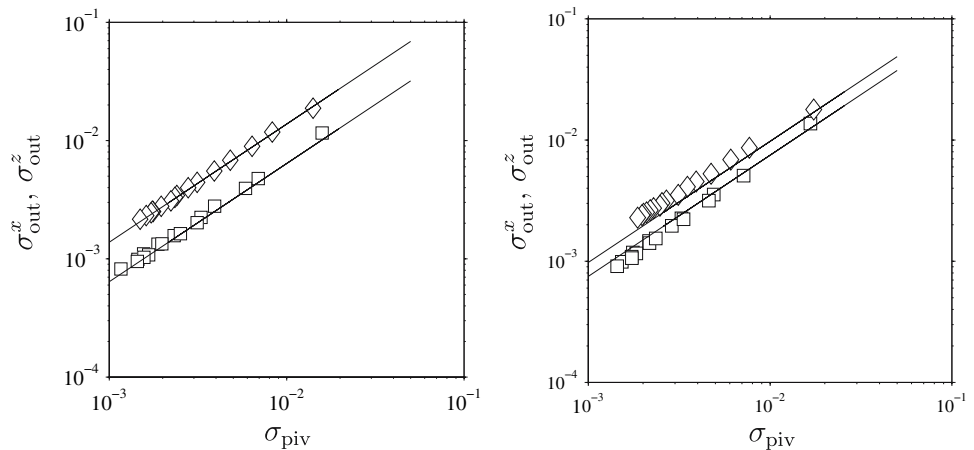


**Table 3** Sensitivity of 3D reconstructed  $\sigma_{out}^x$  and  $\sigma_{out}^z$  to  $\sigma_{in}^x$  for symmetric  $30^\circ$  and  $45^\circ$  cases with both two and three cameras

	$3c_{\sigma_{out}^x}$	$2c_{\sigma_{out}^x}$	$3c_{\sigma_{out}^z}$	$2c_{\sigma_{out}^z}$
$30^\circ$	0.640	1.000	1.383	1.732
$45^\circ$	0.750	1.000	0.976	1.000

Note the sensitivity of the  $\delta x$  component is reduced while the sensitivity of the  $\delta z$  component is unchanged

improvement in the sensitivities of the  $\delta x$  and  $\delta y$  components are apparent when using three cameras.

## 5 Comparison with CFD of confined vortex breakdown

The flow within a closed cylindrical cavity with a rotating lid is considered. This type of flow has been the focus of earlier studies (see for example Vogel 1968; Escudier 1984; Lopez 1990; Sørensen and Christensen 1995; Spohn et al. 1998). Surprisingly, this flow has not been measured experimentally in a quantitative manner, with more than two velocity components. A similar flow has been measured at FLAIR (Dusting et al. 2006), however, this was for the particular case with a free surface. Due to the simple geometry of the closed cavity and the existence of efficient axisymmetric Navier–Stokes solvers, this type of problem is highly suitable as a benchmark for all SPIV measurements. The simulation presented here was produced by an axisymmetric DNS solver. A detailed description of the formulation and numerical implementation can be found in Sørensen and Loc (1989).

### 5.1 Experimental setup

As shown in Fig. 12, the experimental apparatus consisted of an octagonal shaped container. A circular cylinder (radius  $R = 32.5$  mm) was placed in its center. The aspect

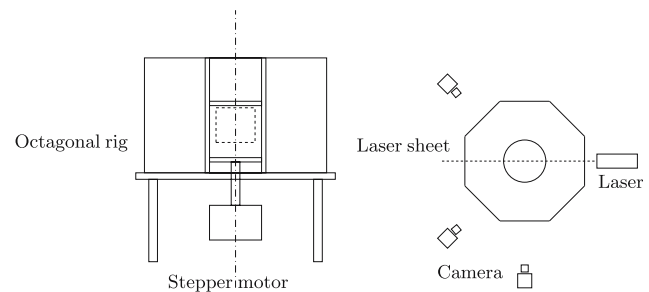


**Fig. 12** Schematic diagram of the experimental apparatus. Left side-view, where the dashed window shows the measured region. Right top-view showing apparatus and position layout of the laser sheet and the cameras. Note the octagonal shaped rig used to reduce distortion and the symmetric layout of the cameras about the laser sheet

ratio (height to radius), of the cylindrical cavity ( $H/R$ ) is controlled by varying the position of the top disk. The octagonal shape allows the exterior faces of the rig to be flat in order to reduce refraction effects that result in optical distortion errors during the use of image-based measurement techniques. A flat, circular disk acted as the rotating bottom, and was located in the center of the base. The disk was rotated by means of a stepper motor and high-performance motion controller (National Instruments, USA).

The Stereo PIV technique detailed in Sect. 2 was used to measure this flow. Imaging was performed using three PixelFly (PCO, Germany) cameras with a resolution of  $1,360 \times 1,024$  pixels. Magnification of 20.4 px/mm resulted in the relatively large field of view as shown schematically with dashed lines in Fig. 12. The stereo configuration used was  $\beta_L = -45^\circ$  and  $\beta_R = 225^\circ$ . Illumination was provided by a QuantaRay (SpectraPhysics, USA) double pulsed NdYag Laser, focused into a 1 mm thin light sheet. The tracer particles used were Spherulac (Potters Industries, USA), silver coated hollow glass microspheres with a nominal diameter of 14  $\mu\text{m}$  and specific gravity of 1.6 (Fig. 13).

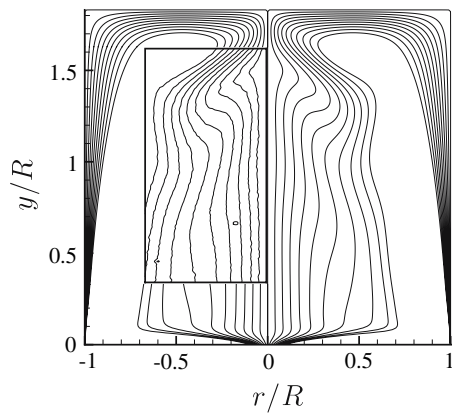


**Fig. 13** Comparison of matched iso-contours for the out-of-plane velocity component between symmetric experimental data (in the boxed region) and numerical data (in the surrounding region)

PIV analysis was performed (see Fig. 2b) with a multi-window iterative analysis, a final window size of  $16 \times 16$  px and a spacing between sampling windows of  $8 \times 8$  px. As the flow was steady images pairs were analysed using correlation averaging to produce more accurate results.

### 5.2 Results and discussion

The Reynolds number based on the the radius of the cavity and the tip speed of the rotating lid is defined as  $Re = \omega R^2 / \nu$ , where  $\nu$  is the kinematic viscosity of the fluid. Data presented here are taken from experiments conducted at  $Re = 2,200$  and  $H/R = 1.85$ . Under these conditions, the flow is steady and contains one vortex breakdown (Escudier 1984). For the sake of brevity, this paper will focus on the out-of-plane component since this is the reconstructed component.

In these types of flow, it has been found that even the slightest imperfections in the apparatus will create asymmetries (Thompson and Hourigan 2003). In order to validate against an axisymmetric CFD simulation, flow measurements have been averaged to produce symmetric data. All experimental data are non-dimensionalised with the previously defined characteristic scales to allow direct comparison with numerical results.

Figure 14 shows the comparison of matched iso-contours for the out-of-plane velocity component between symmetric experimental data (in the boxed region) and numerical data (in the surrounding region). Note the excellent agreement between the numerical and the experimental data. It should be recall that there is no smoothing or filtering of the experimental data from the SPIV process. The PDF of the relative error of these data is shown in Fig. 14. As a direct result of the enforced symmetry, the

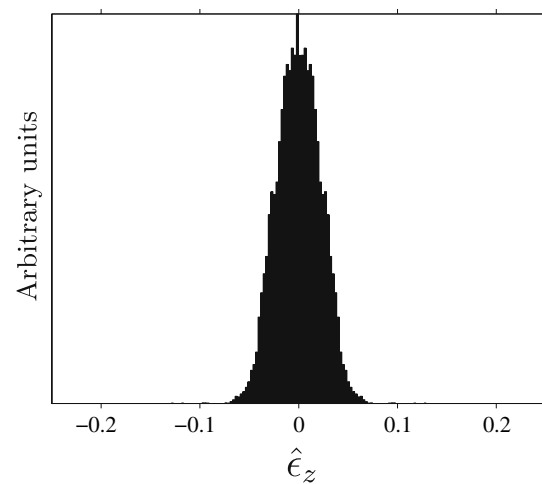


**Fig. 14** Probability density function of the  $\delta z$  component of relative velocity error ( $\hat{\epsilon} = (\mathbf{u}_{exp} - \mathbf{u}_{num}) / \max(\mathbf{u}_{num})$ ). The Gaussian nature of this error is clearly visible

PDF shows no bias error. However, the Gaussian nature of the errors and the low magnitude of these errors can be clearly seen.

Tabulated data of the errors for all three velocity components are presented in Table 4. The bias and standard deviations indicate the high degree of accuracy to which the flow has been measured. Also shown are the  $\Delta\mu$  and  $\Delta\sigma$  values which are the relative differences introduced by setting one of the MFs to null. Note that unlike the translation and rotation cases shown in Table 2, the change is significant when compared to data with the correct MFs. This demonstrates that when the mapping process has errors introduced, errors of similar magnitude appear in the reconstructed errors. The confined swirling flow (combined with its evaluation with CFD) is therefore a candidate as a benchmark flow for Stereo PIV.

As discussed in Sect. 2, the least-squares solution not only provides a highly accurate solution for the reconstructed vector field but also a useful residual. In Fig. 9, it was shown that the mean of the residual,  $\mu(\chi)$ , should be an reliable indicator of the accuracy of the experimental

**Table 4** Table of numerical values of relative bias and standard deviation ( $\sigma$ ) associated with the confined vortex breakdown, at  $Re = 2,200$ , when compared to numerical simulation

	$\mu (10^{-2})$	$\Delta\mu (\%)$	$\sigma (10^{-2})$	$\Delta\sigma (\%)$
$\hat{\epsilon}_x$	NA	NA	4.38	24.06
$\hat{\epsilon}_y$	-1.84	41.51	3.49	27.62
$\hat{\epsilon}_z$	NA	NA	2.21	54.90

Also shown are the  $\Delta\mu$  and  $\Delta\sigma$  values which are the differences introduced by setting one of the MFs to null. Note that the change is significant when compared with data with the correct MFs

**Table 5** Table of the accuracy of the predicted errors for the rotational case presented in Sect. 3 and the vortex breakdown case

	$\mu(\chi)$	Predicted $\ \sigma_{\text{out}}\ $	Measured $\ \sigma_{\text{out}}\ $
Rotation case	0.1227	0.1003	0.1091
Vortex breakdown case	0.3623	0.2961	0.3230

Predicted  $\|\sigma_{\text{out}}\|$  is the product of  $\mu(\chi)$  and the value of the gradient of the Monte Carlo simulation shown in Figs. 9 and 10d at the appropriate angles

results. For a particular configuration, Fig. 10d provides the practitioner with  $\|\sigma_{\text{out}}\|/\mu(\chi)$ . Therefore it is a trivial task to obtain a estimate of the measurement error by multiplying this value by the  $\mu(\chi)$  valued obtained during the application of the reconstruction process to experimental data. Table 5 illustrates the usefulness of the mean residual  $\mu(\chi)$ . The accuracy of the predicted errors for the rotational case presented in Sect. 3 and the vortex breakdown case is given. The reader will appreciate the good agreement between the predicted and the measured error. The measured errors are slightly underestimated, a fact readily explained by the absence of calibration and other systematic, non-random errors in the Monte Carlo analysis.

## 6 Conclusions

A novel, accurate and simple Stereo PIV technique utilising three cameras has been presented. The key feature of the new technique is the elimination of a separate calibration phase. The calibration data are measured concurrently with the PIV data by a third paraxial camera. This has the benefit of improving ease of use and reducing the time taken to obtain data. These benefits can be achieved only if the paraxial view can be imaged with minimal distortion, which is in general the case, but for complex geometries distortion can often be minimised, for example, with the octagonal shaped rig as used in this study.

The new technique is rigorously validated using both pure translation and rotation test cases. However, while this kind of validation is standard, it is shown that such validation is substantially limited and an improved validation process is required.

This third camera also provides useful velocity information, significantly improving the accuracy of the resolved 3D vectors. It has been found that a fixed improvement of  $\sqrt{2/3}$  improvement in the accuracy of the  $\delta y$  component can be achieved. Similar improvements (which are a function of camera stereo angles) are achieved for the  $\delta x$  and  $\delta z$  vector components.

The use of a least-squares approach to the solution of the reconstruction equations further improves the utility of

the technique by providing a robust and useful residual. While it has been shown that on an individual vector basis the residual is not meaningful, thorough error analysis shows that on a global basis this residual is an accurate predictor of resolved vector errors. This powerful predictive tool could possibly be used in conjunction with techniques other than that suggested here, provided it solves the reconstruction process with a least-squares process.

**Acknowledgments** The authors wish to thank Professor Jens Sørensen for his advice, help and the use of his code. DL thanks the Swiss National Science Foundation for their support.

## References

- Arroyo M, Greated C (1991) Stereoscopic particle image velocimetry. *Meas Sci Technol* 2:1181–1186
- Chen J, Katz J (2005) Elimination of peak-locking error in PIV analysis using the correlation mapping method. *Meas Sci Technol* 16:1605–1618
- Dusting J, Sheridan J, Hourigan K (2006) A fluid dynamics approach to bioreactor design for cell and tissue culture. *Biotechnol Bioeng* 94:1196–1208
- Escudier M (1984) Observations of the flow produced in a cylindrical container by a rotating endwall. *Exp Fluids* 2:189–196
- Fouras A, Soria J (1998) Accurate out-of-plane vorticity calculation from in-plane velocity vector field data. *Exp Fluids* 25:409–430
- Fouras A, Dusting J, Hourigan K (2007) A simple calibration technique for stereoscopic particle image velocimetry. *Exp Fluids* 42:799–810
- Hori T, Sakakibara J (2004) High-speed scanning stereoscopic PIV for 3d vorticity measurement in liquids. *Meas Sci Technol* 15:1067–1078
- Lawson N, Wu J (1997) Three-dimensional particle image velocimetry: experimental error analysis of a digital angular stereoscopic system. *Meas Sci Technol* 8:1455–1464
- Lindken R (2006) Stereoscopic micro particle image velocimetry. *Exp Fluids* 41:161–171
- Lopez J (1990) Axisymmetrical vortex breakdown. Part 1. Confined swirling flow. *J Fluid Mech* 221:533–552
- Meinhart CD, Werely ST, Santiago JS (2000) A PIV algorithm for estimating time-averaged velocity fields. *J Fluids Eng* 122:285–289
- Meunier P, Leweke T (2003) Analysis and minimization of errors due to high gradients in particle image velocimetry. *Exp Fluids* 35:408–421
- Perret L, Braud P, Fourment C, David L, Delville J (2006) 3-Component acceleration field measurement by dual-time stereoscopic particle image velocimetry. *Exp Fluids* 40:813–824
- Prasad A (2000) Stereoscopic particle image velocimetry. *Exp Fluids* 29:103–116
- Prasad A, Adrian R (1993) Stereoscopic particle image velocimetry applied to liquid flows. *Exp Fluids* 15:49–60
- Press WH, Flannery BP, Teukolsky SA, Vetterling WT (1992) *Numerical recipes in C: the art of scientific computing*, 2nd edn. Cambridge University Press, Cambridge
- Raffel M, Willert CE, Kompenhans J (1998) *Particle image velocimetry: a practical guide*. Springer, Berlin
- Scarano F, David L, Bsibsi M, Calluaud D (2005) S-PIV comparative assessment: image dewarping + misalignment correction and pinhole + geometric back projection. *Exp Fluids* 39:257–266

- Schroder A, Kompenhans J (2004) Investigation of a turbulent spot using multi-plane stereo particle image velocimetry. *Exp Fluids* 36:82–90
- Soloff SM, Adrian RJ, Liu ZC (1997) Distortion compensation for generalized stereoscopic particle image velocimetry. *Meas Sci Technol* 8:1441–1454
- Sørensen J, Christensen E (1995) Direct numerical simulation of rotating fluid-flow in a closed cylinder. *Phys Fluids* 7(4):764–778
- Sørensen JN, Loc TP (1989) High-order axisymmetric Navier–Stokes code: description and evaluation of boundary conditions. *Int J Num Methods Fluids* 9:1517–1537
- Spohn A, Mory M, Hopfinger E (1998) Experiments on vortex breakdown in a confined flow generated by rotating disk. *J Fluid Mech* 370:73–99
- Thompson MC, Hourigan K (2003) The sensitivity of steady vortex breakdown bubbles in confined cylinder flows to rotating lid misalignment. *J Fluid Mech* 496:129–138
- Vogel H (1968) Experimentelle ergebnisse über die laminare strömung in einem zylindrischen gehäuse mit darin rotierender scheinbe. Bericht 6, Max–Planck-Institut für Strömungsforschung, Göttingen
- Wieneke B (2005) Stereo-PIV using self-calibration on particle images. *Exp Fluids* 39:267–280
- Willert C (1997) Stereoscopic digital particle image velocimetry for application in wind tunnel flows. *Meas Sci Technol* 8:1465–1479